SAND2022-3545J

Electrodeposition of complex high entropy oxides via water droplet formation and conversion to crystalline alloy nanoparticles.

Stephen J. Percival,[+,*] Ping Lu,[^] Daniel R. Lowry,[+] Tina M. Nenoff[#,*]

[+] Sandia National Laboratories, Electronic, Optical and Nano Materials Department, Albuquerque, New Mexico 87185, United States

[^] Sandia National Laboratories, Materials Characterization and Performance Department, Albuquerque, New Mexico 87185, United States

[#] Sandia National Laboratories, Materials Chemicals and Physics Center, Albuquerque, New Mexico 87185, United States

*sperciv@sandia.gov *tmnenof@sandia.gov

KEYWORDS: Nanoparticles, Ligand Free, High Entropy Oxide, Electrodeposition, Emulsion Collisions, Thermal Reduction, Oxygen Evolution Reaction.

ABSTRACT: A combination of electrodeposition and thermal reduction methods have been utilized for the synthesis of ligand free FeNiCo alloy nanoparticles through a high entropy oxide intermediate. These phases are of great interest to the electrocatalysis community, especially when formed by a sustainable chemistry method. This is successfully achieved by first forming a complex five element amorphous FeNiCoCrMn high entropy oxide (HEO) phase via electrodeposition from a nanodroplet emulsion solution of the metal salt reactants. The amorphous oxide phase is then thermally treated and reduced at 570 – 600 °C to form the crystalline FeNiCo alloy with a separate $CrMnO_x$ co-phase. The FeNiCo alloy is fully characterized by scanning transmission electron microscopy and energy-dispersive x-ray spectroscopy elemental analysis and is identified as a face-centered cubic crystal with the lattice constant a = 3.52 Å. The un-optimized, ligand free FeNiCo NPs activity towards the oxygen evolution reaction is evaluated in alkaline solution and found to have an ~185 mV more cathodic onset potential than Pt metal. Beyond being able to synthesize highly crystalline, ligand free FeNiCo nanoparticles, the demonstrated and relatively simple two-step process is ideal for the synthesis of tailor-made nanoparticles where the desired composition is not easily achieved with classical solution-based chemistries.

INTRODUCTION

New approaches to the tuned synthesis of target composition catalysts is important to sustainable materials development.[1,2] The alloying of key elements into a homogenous alloy further enables both the reactivity and the performance through high surface area phases.[3-5] New electrocatalyst synthesis methods in which advances in control over the catalyst formation and composition will lead to designer catalysts with higher activity, stability and faradaic efficiency, ultimately affecting costs and process sustainability.[2,6,7]

Efficient electrocatalysts are being pursued due to their use in sustainable energy conversion and storage processes. Examples of this include water electrolysis,[8] artificial photosynthesis,[9] and metal-air batteries.[10,11] Many complex, multistep, electrocatalytic reactions, including the oxygen evolution reaction (OER) or the nitrogen reduction reaction (NRR) suffer from slow kinetics, low faradaic efficiencies, or both and require the continued development of complex novel catalyst materials.[12,13] There is a great interest in the field to move away from noble metals which can be prohibitively expensive, such as Ir or Ru based materials for OER, to use more earth abundant transition metals, and the alloys of transition metals.[14-16] However, the focus is on optimizing a complex mixed composition to enhance the activity while maintaining high surface area and the compositional integrity of the alloy.[17]

One promising alloy composition for OER is the FeNiCo-based alloy composition. Usually, these alloys are synthesized via chemical methods such as chemical vapor deposition (CVD), electrodeposition, or co-precipitation[18-20] or require the additional consumption of excess chemicals (such as the polyol or glycine-nitrate reactions).[21,22] Notably, many of these synthesis techniques result in carbon or silica phase supported nanoparticles (NPs), originating from the support and CVD process. Saha et.al.,[17] have reported a synthetic route that uses metal layered double hydroxides (LDH) precursors that are calcined to the pure nanoparticle alloy.

Long, et.al.,[23] have recently shown that the FeCoNi alloy in the face-centered cubic (FCC) phase, can be made by mechanical alloying and spark plasma sintering. Importantly, they showed that by incorporating an additional two elements into the alloy composition, they successfully synthesize a high entropy alloy (HEA) of $FeCoNi(CuAl)_x$ composition that transitions to a body-centered cubic (BCC) phase when x = 0.4 ~1.0. While this process is less sustainable than other processes, it shows a reaction pathway to forming not only the FeNiCo alloy for OER, but also to forming chemically and mechanically interesting HEAs with improved properties such as high tensile strength or oxidation resistance. However, this process does not form nanoparticles which are highly desirable for their large surface area and high surface energies, important considerations for catalysts with high activity.

With the need for new, versatile synthesis processes, herein, we report a novel reaction pathway to synthesize unique ligand free

multi-element-alloy NPs for catalytic applications. In particular, we use the FeNiCo alloy as an example of how that pathway occurs: the electrochemical formation of an unstable 'intermediate' amorphous FeNiCoCrMn HEA oxide phase which easily reduces with temperature to the thermodynamically stable target nanoparticle FeNiCo alloy of interest. Furthermore, it gives insights into future pathways for the formation of five-element HEA nanoparticle catalysts. This is particularly interesting in light of recent reports on the catalytic HEA NPs for ammonia decomposition,[24] electrosynthesis of high entropy metallic glass NPs,[25] and (CrFeMoNbZr)O_2 amorphous films.[26]

EXPERIMENTAL METHODS

Reaction Chemistry. All chemicals were purchased and used without further purification. The reaction conditions used were similar to those found in the literature.[25] 1,2-Dichloroethane (DCE, Sigma Aldrich, ACS Reagent >99.0%), tetrabutylammonium tetrafluoroborate ($TBABF_4$, Sigma Aldrich, 99%), nickel chloride ($NiCl_2{\cdot}6H_2O$ Alfa Aesar, 99.95%), cobalt chloride ($CoCl_2{\cdot}6H_2O$, Alfa Aesar, 98%), iron chloride ($FeCl_3{\cdot}6H_2O$ Alfa Aesar, ACS 97-102%) manganese chloride ($MnCl_2{\cdot}4H_2O$, Acros Organics, >99%), chromium chloride ($CrCl_3{\cdot}6H_2O$, Alfa Aesar, 98%), potassium hydroxide (KOH, Sigma-Aldrich, ACS Reagent grade, >85%) and ethanol (200 proof, Pharmco-Aaper). Aqueous solutions were made in 18.2 MΩ*cm DI water.

Fresh solutions of the individual metal ion precursors were made at 200 mM concentrations using deionized H_2O and diluted to the desired concentrations before use. The metal ion solutions were diluted and combined to a final concentration of 40 mM total metal ion concentration (8 mM concentration for each specific metal cation to achieve the equimolar nanoparticle composition). Nanodroplet emulsion solutions were made by adding 60 µL of the 40 mM metal ion precursor solution to 10 mL of DCE with 100 mM $TBABF_4$ solution. This immiscible solution was then ultrasonicated using a horn ultrasonicator (500 W, 20 kHz, Qsonica L.L.C., Newtown, CT) equipped with a ¼" diameter tip at 40% amplitude for 10 on-off cycles of 5 seconds on and 5 seconds off. This was then quickly added to the electrochemical cell for deposition onto an electrode surface.

Electrochemical Nanoparticle Growth. Electrochemical experiments were performed in a standard 3-electrode configuration using a Gamry Reference 600+ potentiostat. A large area sheet of Pt foil was used as the counter electrode, and a commercially available Ag/AgCl electrode (Bioanalytical Systems Inc.) was used for the reference.

The working electrodes consisted of carbon-fiber ultra-microelectrodes, UMEs, (Bioanalytical Systems Inc., 11±2 µm diameter) Highly Oriented Pyrolytic Graphite (HOPG, Structure Probe Inc. Supplies), Glassy Carbon (GC, Type 1, Alfa Aesar) or for microscopy analysis, carbon-coated molybdenum transmission electron microscopy (TEM) support grids (Support Films, Carbon 200 mesh, Mo, Ted Pella, Inc.). Carbon-fiber UMEs used for initial determination of nanodroplet collision and deposition were polished on (1200 grit) silicon carbide polishing paper, then polished on a nylon polishing pad with 0.05 µm alumina suspension, and finally sonicated in DI water to remove any alumina particles. The HOPG was freshly cleaved before deposition to ensure a clean, atomically smooth surface for SEM imaging. The GC was cut into 1cm^2 squares and sonicated to remove any debris from the cutting procedure. The potential was biased to a suitable negative potential to deposit and attempt to reduce the metal salts onto the substrate, typically ≤ -1.5 V (vs. Ag/AgCl) for 180 seconds duration. The amorphous HEO NPs were electrochemically deposited directly onto TEM grids for electron microscopy and elemental analysis. TEM grids were held with a toothless alligator clip to electrically connect them to the potentiostat leads and gently suspended over the solution so only the TEM grid was in the deposition solution and to try to prevent the clip from also being in contact with the solution. After deposition, the samples were cleaned by first immersing them in ethanol for 5 minutes and then in DI water for 5 minutes to remove the organics and any remaining salts from the sample surface. A similar procedure was used for both the HOPG and GC substrates. The GC substrates with the electrochemically deposited NPs were placed in a custom-built electrochemical test cell with a kalrez o-ring defining a uniform area of 0.7088 cm^2 for the OER testing in 0.1 M KOH solution (pH measured to be 13). Thermal annealing of NPs on HOPG or GC substrates was performed in a quartz tube furnace under a 200 sccm flow of argon at 600 °C for 60 minutes followed by a furnace quench back to room temperature.

Scanning Electron Microscopy (SEM) and Scanning Transmission Electron Microscopy (STEM). Scanning electron microscopy (SEM) analyses were captured on a FEI Nova Nano SEM 230, at various accelerating voltages between 1 and 20 kV. A FEI Titan™ G2 80-200 STEM with a Cs probe corrector and ChemiSTEM™ technology (X-FEG™ and SuperX™ EDS with four windowless silicon drift detectors) operated at 200 kV was used in this study. Energy-dispersive x-ray spectroscopy (EDS) and Z-contrast or high-angle annular dark-field (HAADF) imaging were used for compositional and structural analysis, respectively. The EDS spectral imaging was acquired as a series of frames, where the same region was scanned multiple times. An electron probe of size of about 0.13 nm, convergence angle of 18.1 mrad, and current of ~75 pA was used for the EDS acquisition. EDS spectral imaging was analyzed by multivariate analysis using the principal component analysis (PCA) method.[27] The compositional analysis utilized Cliff and Lorimer method.[28] HAADF images were recorded under similar optical conditions using an annular detector with a collection range of 60-160 mrad.

Thermal reduction of nanoparticle oxides for TEM analysis was performed via in-situ TEM experiments using a Gatan heating TEM holder. The sample on the Mo TEM gird was heated inside TEM (a vacuum pressure of about $1x10^{-6}$ torr) from room temperature to 570 °C in 10 minutes, hold at 570 °C for 50 minutes and cooled to room temperature in 2 minutes. EDS and imaging analysis of the after-heated samples were carried at room temperature.

RESULTS AND DISCUSSION

The reaction pathway described herein begins with the electrosynthesis of amorphous five component metal oxide NPs followed by thermal annealing to crystallize to ternary alloy NPs. The amorphous oxide NP electrosynthesis process first involves formation of an emulsion of aqueous nanodroplets (which contain the reactant metal ions dissolved in the water) freely diffusing through an immiscible organic phase. This electrosynthesis procedure utilizes a solution system that was pioneered by Bard and co-workers,[29-32] which is slightly modified to achieve NP deposition.[33,34] These nanodroplets, formed in the water-in-oil emulsion mixture, are found to be ~450 nm in diameter after ultrasonication of the precursor mixture.[25] Nanoparticle deposition occurs on a suitably biased electrode when inserted into the emulsion as the individual nanodroplets collide with the electrode surface and the metal precursors are reduced at the at the electrode forming an amorphous particle, as seen in Figure 1a.

An example amperometric trace from an 11 µm-diameter carbon-fiber UME is shown in Figure 1b. The sudden, stochastic current spikes indicate the collision of an aqueous nanodroplet with the

electrode surface. Each collision event (current spike) indicates the synthesis of a new metal-containing oxide particle. The amount of charge passed under each current spike is proportional to the size of the colliding droplet, the initial concentration of the reactants and can be proportional to the amount of material deposited.[25,35] It is at that point that the newly formed amorphous FeNiCoCrMn HEO phases can be found in TEM analysis.

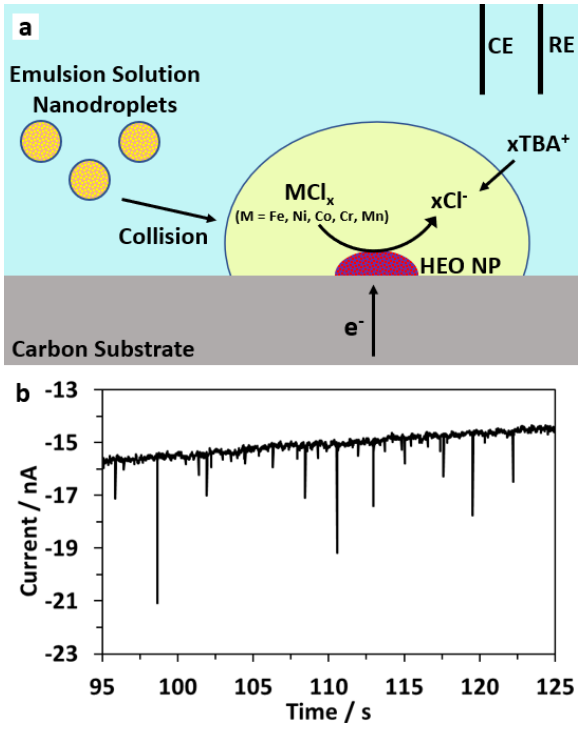

Figure 1. (a) Schematic showing the generalized HEO NP deposition resulting from a nanodroplet collision on the electrode. (b) Example amperometric trace from a carbon fiber UME in the emulsion deposition solution. Applied potential was -1.5 V vs. Ag/AgCl.

Post electrosynthesis, STEM HAADF imaging and EDS analysis of the major reaction phase present in the NP sample confirm the presence an amorphous oxide phase, shown in Figures 2 and 3. The presence of reaction elements of Fe, Ni, Co, Cr and Mn are evident by EDS mapping (see Figure 3b), and the formation of the HEO and not a metallic alloy is confirmed by the abundance of oxygen also present in the EDS (Figure 3c). We postulate that the metals are being reduced during the duration of the experiment but then subsequently re-oxidize to the HEO. This can result from either from being in contact with water (after the applied potential is removed) or through reaction with ambient oxygen. However, at this time, neither has been confirmed. Note, the minor presence of Al Cl, Ca and Si are attributed to metal salt impurities. The Mo peak in the EDS spectrum, on the other hand, is due to the Mo TEM grid used. The nanoparticles have a composition of approximately $Fe_{1.0}$ $Ni_{1.0}Co_{1.0}Cr_{1.0}Mn_{0.95}$. (See Figure 3)

The metal ratio in the oxide can be controlled by varying the concentration in the aqueous solution. Shown above, the HEO with nearly equal atomic ratio was achieved. By contrast, a controlled high Co concentration sample was also obtained (see Supporting Information, Figure S1). By increasing the concentration of Co in the reaction mixture, a final high ratio Co content amorphous HEA oxide NP of composition $Fe_{1.0}$ $Ni_{0.8}Co_{1.5}Cr_{1.0}Mn_{1.0}$ was produced.

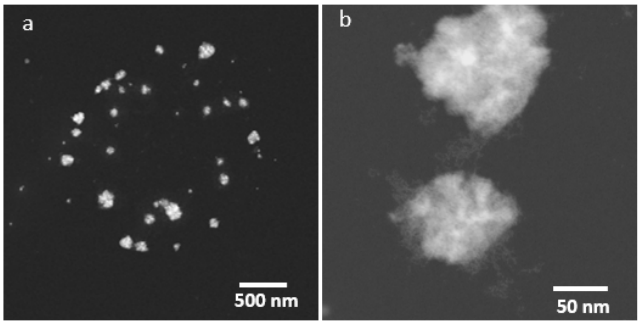

Figure 2. STEM HAADF images of the solution synthesized HEO NPs at two magnifications (a, b).

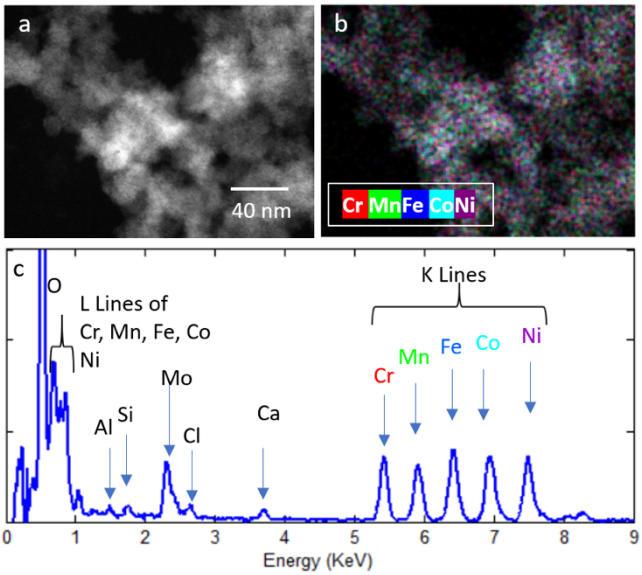

Figure 3. STEM imaging and EDS analysis of FeNiCoCrMn oxide phase. (a) HAADF image; (b) EDS composite color maps and (c) summed EDS spectrum from the particles. The HEO has an estimated cation composition of $Fe_{1.0}Ni_{1.0}Co_{1.0}Cr_{1.0}Mn_{0.95}$.

At this point in the reaction process, the reactants have been fully mixed into this new 'intermediate' oxide amorphous phase. The reactivity of this phase to the formation of alloy NPs was then explored. The thermodynamic metastability of amorphous oxides[22] enabled the reduction of the phase to a fully metal-based alloy via heating. The sample, still on the grid, underwent an in-situ heating step. The process resulted in the crystallization of the nanoparticles into two partially segregated phases: a crystalline FeNiCo alloy and a $CrMnO_x$ co-phase. The detection of crystallinity and accompanying change in the particle morphology were observed at a temperature of about 570°C. Figure 4 shows the HAADF images after in-situ heating at 570°C for 60 minutes. The FeNiCo NPs appear as bright-particles with size of 2-50 nm and are in mixture with the $CrMnO_x$ phase (a darker, cloud-like phase in between the bright particles). Similarly, a morphology change was observed for the HEO NPs deposited on HOPG and annealed under flowing Ar at 600 °C, as seen in the Supporting Information Figure S2.

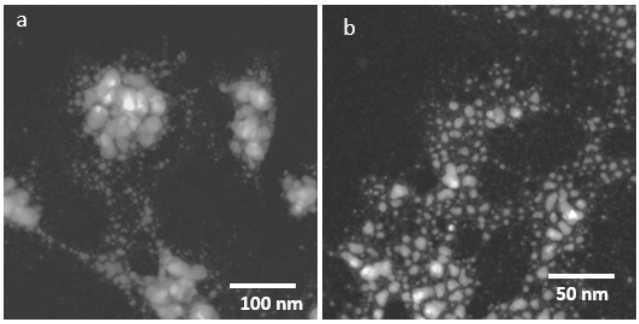

Figure 4. STEM HAADF images of the FeNiCoCrMn oxide phase after annealing at 570°C for 60 minutes, showing the formation of the FeNiCo (bright) NPs with various sizes (2 nm - 50 nm) mixed with the $CrMnO_x$ phase.

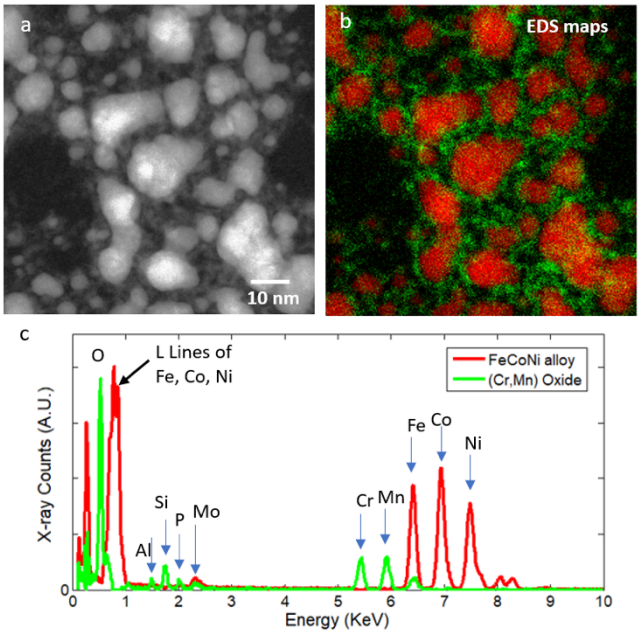

Figure 5. STEM imaging and EDS analysis of FeNiCoCrMn oxide phase after annealing at 570°C for 60 minutes. (a) HAADF image; (b) EDS color maps displayed according to two principal components derived from the PCA analysis (Component 1, the FeNiCo phase in red; Component 2, the $CrMnO_x$ phase in green); and (c) EDS spectra of the two PCA components.

The presence of two phases is confirmed by EDS mapping and PCA analysis (Figure 5). These phases are composed of metallic FeNiCo NPS and an oxide of CrMnOx surrounding the metallic particles. The oxide phase may help stabilize the metallic NPs during the anneal preventing Ostwald ripening. The $CrMnO_x$ phase contains minor content of Al, Si, P, initially present in the original HEO NP oxide phase. The FeNiCo alloy has an estimated composition $Fe_{1.0}Co_{1.1}Ni_{0.8}$. The crystalline nature of the FeNiCo was revealed by high-resolution HAADF image shown in Figure 6. The inset FFT pattern of a NP shows the FeNiCo particle has a face-centered cubic (FCC) structure with a lattice constant of 3.52 Å.

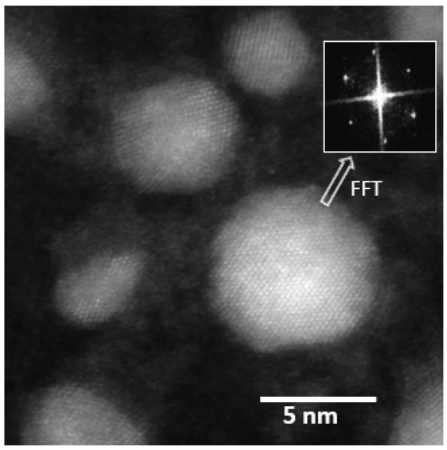

Figure 6. High-resolution STEM HAADF image of the FeNiCo NPs formed by the annealing. The lattice fringes and inset FFT pattern from a NP were used to determine the crystal structure to be the FCC with a = 3.52 Å.

The electrocatalytic activity of the annealed FeNiCo NPs was evaluated for the OER in alkaline solutions. The Linear Sweep Voltammetry (LSV) results from the OER experiments on bare GC, Pt foil, HEO NPs and the thermally reduced NPs are presented in Figure 7. The HEO NP precursor (equimolar FeNiCoCrMn) was deposited on GC substrate and then thermally annealed to reduce the particles to the desired FeNiCo metallic phase. The substrates were then placed in an electrochemical cell with a well-defined orifice for OER testing. The as-deposited HEO NPs LSV showed an initial increase in current at a similar potential as the thermally reduced FeNiCo NPs but couldn't achieve the standard 10 mA/cm^2 oxidation current typically used to as the measure of the onset potential. The LSV current is seen to reach a peak current and then drop down where it then begins following the current profile seen for the Bare GC. This initial current wave is not entirely surprising since the HEO NPs still contain the electrochemically active elements (as oxides) that will participate as active sites for the OER reactions. This deactivation could be due to either: poisoning of the small number of available active sites on the surfaces of the oxide nanoparticles, or the agglomeration of the nanoparticles as the potential is increased forming larger particles with a lower total electrocatalytically active surface area. The thermally reduced FeNiCo NPs however, did not show a similar drop in the current and are seen to quickly increase the current beyond the 10 mA/cm^2 onset potential. The LSV onset potential is measured as 0.905 V (vs. Ag/AgCl) for the FeNiCo NPs compared to 1.087 V (vs. Ag/AgCl) for the Pt foil, which is more than 182 mV more cathodic.

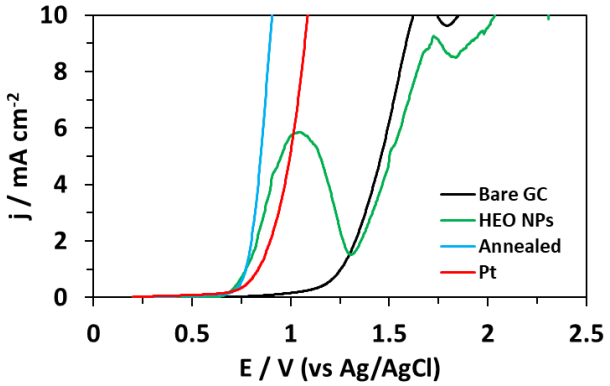

Figure 7. Evaluation of the OER for the as made HEO NPs, the annealed (FeNiCo) NPs, bare GC and Pt foil in 0.1 M KOH solution. LSV scan rate was 10 mV/s.

The unique combination of analytical methods has confirmed the formation of electrocatalytically active FeNiCo alloy nanoparticles via electrodeposition and low temperature annealing. These non-optimized particles have already been shown to be highly active for the OER and may be further tuned to achieve increased performance. This confirms the ability to follow a reaction pathway through complex 'intermediate' amorphous phases to more thermodynamically stable functional alloy phases as the final reaction product.

CONCLUSION

Herein, we report a novel reaction pathway to synthesize unique multi-element-alloy NPs for catalytic applications. A FeNiCo alloy was used as an example of how that pathway occurs: the electrochemical formation of an 'intermediate' amorphous FeNiCoCrMn HEO phase which easily reduces with temperature to the target nanoparticle FeNiCo alloy of interest.

Specifically, an emulsion nanodroplet collision electrodeposition method enabled the mixing of the FeNiCoCrMn components which then formed into an amorphous HEO phase. Composition and non-crystallinity were confirmed by STEM-EDS. The same sample was then easily reduced at 570-600 °C to the target nanoparticle FeNiCo alloy of interest with the amorphous co-phase of $CrMnO_x$ present in this final product. Interestingly, this is the only reaction process reported that results in the synthesis of a ligand free FeNiCo alloy nanoparticle directly through a primarily wet chemistry method followed by a fast, thermal annealing step. The activity of the as made HEO NPs and the thermally reduced FeNiCo alloy NPs was evaluated for the OER in alkaline solutions. While the HEO NPs do show some tendency to catalyze the OER they do not demonstrate a high stability and quickly deactivate, whereas the thermally reduced FeNiCo NPs are more stable and reveal a much lower onset potential compared to Pt.

The reduction step in this reaction can be considered a relatively low temperature sintering process as compared to other multicomponent alloy nanoparticle sintering temperatures.[26] Beyond being able to synthesize highly crystalline, ligand free FeNiCo nanoparticles, the demonstrated and relatively simple two-step process is ideal for the synthesis of tailor-made nanoparticles where the desired composition is not easily achieved with classical solution based chemistries.[25,36] On-going research is focused on optimizing the temperature to that of the lowest possible for complete reduction of all components in the intermediate phase to the targeted alloy. This thermal treatment extension of the nanodroplet electrodeposition process may open up new avenues for functional nanoparticle synthesis where specific tailoring of particle constituents may be necessary. Future work will focus also on scalability of multicomponent metal alloy nanoparticle formation.[37]

ASSOCIATED CONTENT

Supporting Information.

Additional STEM and EDS data (Figure S1) provided for targeted high Co composition $Fe_{1.0}Ni_{0.8}Co_{1.5}Cr_{1.0}Mn_{1.0}$ and low Cr composition $Fe_{1.0}Ni_{1.3}Co_{1.3}Cr_{0.1}Mn_{1.0}$ amorphous oxide NPs obtained by varying the starting metal concentrations, SEM images of the HEO NPs on HOPG before and after annealing at 600 °C. A histogram plot of the measured size distributions of the metallic FeNiCo nanoparticles. This material is available free of charge via the Internet at http://pubs.acs.org.

AUTHOR INFORMATION

Corresponding Authors

* sperciv@sandia.gov
* tmnenof@sandia.gov

Author Contributions

The manuscript was written through contributions of all authors and all authors have given approval to the final version of the manuscript.

Funding Sources

This work is supported by the Laboratory Directed Research and Development Program at Sandia National Laboratories.

ACKNOWLEDGMENT

The authors thank Dr. Remi Dingreville for his support and technical guidance with this study. Sandia National Laboratories is a multi-mission laboratory managed and operated by National Technology and Engineering Solutions of Sandia, LLC., a wholly-owned subsidiary of Honeywell International, Inc., for the U.S. Department of Energy's National Nuclear Security Administration under contract DE-NA0003525. This paper describes objective technical results and analysis. Any subjective views or opinions that might be expressed in the paper do not necessarily represent the views of the U.S. Department of Energy or the United States Government.

REFERENCES

1. Sardar, R.; Funston, A. M.; Mulvaney, P.; Murry, R. W. Gold Nanoparticles: Past, Present and Future. *Langmuir* **2009**, *25*, 13840-13851. DOI: 10.1021/la9019475.

2. Myers, V. S.; Frenkel, A. I.; Crooks, R. M. In Situ Characterization of Platinum Dendrimer-Encapsulated Oxygen Reduction Electrocatalysts. *Langmuir* **2012**, *28*, 1596-1603. DOI: 10.1021/la203756z.

3. Stamenkovic, V. R.; Mun, B.; Arenz, M.; Mayrhofer, K.J.J.; Lucas, C. A.; Wang, G.; Ross, P.N.; Markovic, N.M. Trends in electrocatalysis on extended and nanoscale Pt-bimetallic alloy surfaces. *Nat. Mater.* **2007**, *6*, 241-247. DOI: 10.1038/nmat1840.

4. Cochell, T.; Manthiram, A. $Pt@Pd_xCu_y/C$ Core-Shell Electrocatalysts for Oxygen Reduction Reaction in Fuel Cells. *Langmuir* **2012**, *28*, 1579-1587. DOI: 10.1021/la202610z.

5. Castegnaro, M. V.; Paschoalino, W. J.; Fernandes, M. R.; Balke, B.; Alves, M. C. M.; Ticianelli, E. A.; Morais, J. Pd-M/C (M = Pd, Cu, Pt) Electrocatalysts for Oxygen Reduction Reaction in Alkaline Medium: Correlating the Electronic Structure with Activity. *Langmuir*, **2017**, *33*, 2734-2743. DOI: 10.1021/acs.langmuir.7b00098.

6. Fernandes, D. M.: Novais, H. C.; Basca, R.; Serp, P.; Bachiller-Baeza, B.; Rodriguez-Ramos, I.; Guerro-Ruiz, A.; Freire, C.

Polyoxotungstate@Carbon Nanocomposites as Oxygen Reduction Reaction (ORR) Electrocatalysts. *Langmuir* **2018**, *34*, 6376-6387. DOI: 10.1021/acs.langmuir.8b00299.

7. Li, L.; Wang, X.; Guo, Y.; Li, J. Synthesis of an Ultrafine CoP Nanocrystal/Graphene Sandwiched Structure for Efficient Overall Water Splitting. *Langmuir* **2020**, *36*, 1916-1922. DOI: 10.1021/acs.langmuir.9b03810.

8. Khan, M. A.; Zhao, H.; Zou, W.; Chen, Z.; Cao, W.; Fang, J.; Xu, J; Zhang, L.; Zhang, J. Recent Progresses in Electrocatalysts for Water Electrolysis. *Electrochem. Energ. Rev.* **2018**, *1***,** 483–530. DOI: 10.1007/s41918-018-0014-z.

9. Kärkäs, M.D.; Verho, O.; Johnston, E.V.; Åkermark, B. Artificial Photosynthesis: Molecular Systems for Catalytic Water Oxidation. *Chem. Rev.* **2014**, *114*, 24, 11863-12001. DOI: 10.1021/cr400572f.

10. Lee, D. U.; Xu, P.; Cano, Z.P.; Kashkooli, A. G.; Park, M.G.; Chen, Z. Recent progress and perspectives on bi-functional oxygen electrocatalysts for advanced rechargeable metal–air batteries. *J. Mater. Chem. A* **2016**, *4*, 7107-7134. DOI: 10.1039/C6TA00173D.

11. Shui, Z.; Liao, X.; Lei, Y.; Ni, J.; Liu, Y.; Dan, Y.; Zhao, W.; Chen, X. MnO_2 Synergized with N/S Codoped Graphene as a Flexible Cathode Efficient Electrocatalyst for Advanced Honeycomb-Shaped Stretchable Aluminum-Air Batteries. *Langmuir* **2020**, *36*, 12954-12962. DOI: 10.1021/acs.langmuir.0c02246.

12. Shi, Q.; Zhu, C.; Du, D.; Lin, Y. Robust noble metal-based electrocatalysts for oxygen evolution reaction. *Chem. Soc. Rev*. **2019**, *48*, 3181-3192. DOI: 10.1039/C8CS00671G.

13. Suryanto, B. H.; Wang, D.; Azofra, L. M.; Harb, M.; Cavallo, L.; Jalili, R.; Mitchell, D. R. G.; Chatti, M.; MacFarlane, D. R. MoS_2 Polymorphic Engineering Enhances Selectivity in the Electrochemical Reduction of Nitrogen to Ammonia. *ACS Energy Lett.* **2019**, *4*, 430-435. DOI: 10.1021/acsenergylett.8b02257.

14. Lu, X.; Zhao, C. Electrodeposition of hierarchically structured three-dimensional nickel–iron electrodes for efficient oxygen evolution at high current densities. *Nat Commun* **2015**, *6***,** 6616. DOI: 10.1038/ncomms7616.

15. Elakkiya, R.; Maduraiveeran Two-Dimensional Earth-Abundant Transition Metal Oxides Nanomaterials: Synthesis and Application in Electrochemical Oxygen Evolution Reaction. *Langmuir,* **2020**, *36*, 4728-4736. DOI: 10.1021/acs.langmuir.0c02246.

16.Qiu, Y.; Xin, L.; Li, W. Electrocatalytic Oxygen Evolution over Supported Small Amorphous Ni-Fe Nanoparticles in Alkaline Electrolyte. *Langmuir* **2014**, *30*, 7893-7901. DOI: 10.1021/la501246e.

17. Saha, S.; Ganguli, A.K. FeCoNi Alloy as Nobel Metal-free Electrocatalyst for oxygen evolution reaction (OER), *ChemistrySelect*, **2017**, *2*(4), 1630-1636. DOI: 10.1002/slct.201601243.

18. Jiang, Z.; Xie, T.; Geng, B. Y.; Wang, G. Z.; Wu, G. S.; Yuan, X. Y.; Meng, G. W.; Zhang, L. D. Synthesis of core-shell nanowires of FeCoNi Alloy core with silicon oxide layers. *Inorg. Chem. Commun.* **2004**, *7,* 812–814. DOI: 10.1016/j.inoche.2004.04.016.

19. Yang, Y. Preparation of Fe-Co-Ni Ternary Alloys with Electrodeposition. *Int. J. Electrochem. Sci.* **2015**, *10*, 5164–5175.

20. Carles, V.; Laurent, C.; Brieu, M.; Rousset, A. Synthesis and characterization of Fe/Co/Ni alloys – MgO nanocomposite powders. *J. Mater. Chem.* **1999**, *9*, 1003–1009. DOI: 10.1039/A809642B.

21. Toneguzzo, P.; Viau, G.; Acher,O. Polyol mediated synthesis of nanoscale MS particles (M = Zn, Cd, Hg). *J. Mater. Sci.* **2000**, *35,* 3767–3784. DOI: 10.1039/B103167H.

22. Xie, Z.; Zhu, W.; Zhu, B.; Xia, C. $Fe_xCo_{0.5-x}Ni_{0.5}$-SDC anodes for low-temperature solid oxide fuel cells. *Electrochem. Acta* **2006**, *51*, 3052–3057. DOI:10.1016/j.electacta.2005.08.039.

23. Long, Y; Li, G.; Liang, X.; Peng, H. Fine-Grained $FeCoNi(CuAl)_x$ High Entropy Alloys: Phase Transformation, Microstructure Evolution and Mechanical Properties. *Front. Mater.* **2020**, 7:537812. DOI:10.3389/fmats.2020.537812.

24. Xie, P.; Yao, Y.; Huang, Z.; Liu, Z.; Zhang, J.; Li, T.; Wang, G.; Shahbazian-Yassar, R.; Hu, L.; Wang, C. *Nat. Commun*. 2019, 10, 4011. DOI: 10.1038/s41467-019-11848-9.

25. Glasscott, M. W.; Pendergast, A.D.; Goines, S.; Bishop, A.R.; Hoang, A.T.; Renault, C.; Dick, J.E. Electrosynthesis of high-entropy metallic glass nanoparticles for designer, multi-functional electrocatalysis. *Nat. Commun*., **2019**, 0:2650. DOI: 10.1038/s41467-019010303-z.

26. Gu, X.; Luan, H.; Yang, X.; Wang, X.; Fang, K.; Li, J.; Jia, Y.; Yao, K.; Zhang, Z.; Chen, N. Formation and Properties of Amorphous Multi-component $(CrFeMoNbZr)O_x$ *Thin Films. Metals*, **2020**, *10*, 599. DOI: 10.3390/met10050599.

27. Kotula, P.G.; Kennan, M.R.; Michael, J.R. Automated analysis of SEM X-ray spectral images: a powerful new microanalysis tool. *Microsc. Microanal.* **2003**, *9*, 1-17. DOI: 10.1017/S1431927603030058.

28. Cliff, G.**;** Lorimer, G. W. The quantitative analysis of thin specimens. *J. Microsc*., **1975**, *103*, 203–207. DOI: 10.1111/j.1365-2818.1975.tb03895.x.

29. Kim, B.-K. Boika, A.; Kim, J.; Dick, J. E.; Bard, A. J. "Characterizing Emulsions by Observation of Single Droplet Collisions – Attoliter Electrochemical Reactors." *J. Am. Chem. Soc.* **2014***, 136*, 4849-4852. DOI:10.1021/ja500713w.

30. Dick, J. E.; Renault, C.; Kim, B.-K.; Bard, A. J. Electrogenerated Chemiluminescence of Common Organic Luminophores in Water Using an Emulsion System. *J. Am. Chem. Soc.* **2014**, *136*, 13546-13549. DOI:10.1021/ja507198r.

31. Kim, B.-K.; Kim, J.; Bard, A. J. Electrochemistry of a Single Attoliter Emulsion Droplet in Collisions. *J. Am. Chem. Soc.* **2015**, *137*, 2343-2349. DOI:10.1021/ja512065n.

32. Lebegue, E.; Anderson, C. M.; Dick, J. E.; Webb, L. J.; Bard, A. J. Electrochemical Detection of Single Phospholipid Vesicle Collisions at a Pt Ultramicroelectrode. *Langmuir* **2015**, *31*, 11734-11739. DOI: 10.1021/acs.langmuir.5b03123.

33. Jeun, Y. E.; Baek, B.; Lee, M. W.; and Ahn, H. S. Surfactant-free electrochemical synthesis of metallic nanoparticles via stochastic collisions of aqueous nanodroplet reactors. *Chem. Commun.* **2018**, *54*, 10052-10055. DOI: 10.1039/c8cc05760e.

34. Pendergast, A. D.; Glasscott, M. W.; Renault, C.; and Dick, J. E. One-step electrodeposition of ligand-free PdPt alloy nanoparticles from water droplets: Controlling size, coverage, and elemental stoichiometry. *Electrochem. Commun.* **2019**, *98*, 1-5. DOI: 10.1016/j.elecom.2018.11.005.

35. Glasscott, M. W.; Dick, J. E. Direct Electrochemical Observation of Single Platinum Cluster Electrocatalysis on Ultramicroelectrodes. *Anal. Chem.* **2018**, *90*, 7804-7808.

36. Nenoff, T.M.; Jacobs, B.W.; Robinson, D. B.; Provencio, P.P.; Huang, J.-Y., Ferreira, S.; Hanson, D. Low Temperature Sintering Uranium Oxide Nanoparticles Synthesized via Radiolysis. *Chem. Mater.*, **2011**, *23*, 5185-5190. DOI: 10.1021/cm2020669.

37. Xizheng, W.; Dong, Q.; Qiao, H.; Huang, Z.; Saray, M.T.; Zhong G.; Lin, Z.; Cui, M.; Brozena, A.; Hong, M.; Xia, Q.; Gao, J.; Chen, G.; Shahbazian-Yassar, R.; Wang, D.; Hu, L. Continuous synthesis of hollow high-entropy nanoparticles for energy and catalysis applications. *Adv. Mater.* **2020**, *32*, 46: 2002853. DOI: 10.1002/adma.202002853.

TOC FIGURE